

Monopole topological resonators

Hengbin Cheng,^{1,2} Jingyu Yang,^{1,2} Zhong Wang,³ and Ling Lu^{1,4,*}

¹*Institute of Physics, Chinese Academy of Sciences/Beijing National Laboratory for Condensed Matter Physics, Beijing 100190, China*

²*School of Physical Sciences, University of Chinese Academy of Sciences, Beijing 100049, China*

³*Institute for Advanced Study, Tsinghua University, Beijing 100084, China*

⁴*Songshan Lake Materials Laboratory, Dongguan, Guangdong 523808, China.*

Among the many far-reaching consequences of the potential existence of a magnetic monopole, it induces topological zero modes in the Dirac equation, which were derived by Jackiw and Rebbi 46 years ago and have been elusive ever since. Here, we show that the monopole and multi-monopole solutions can be constructed in the band theory by coupling the three-dimensional Dirac points in hedgehog spatial configurations through Dirac-mass engineering. We then experimentally demonstrate such a monopole bound state in a structurally-modulated acoustic crystal as a cavity device. These monopole resonators not only support an arbitrary number of degenerate mid-gap modes, but also offer the optimal single-mode behavior possible — whose modal spacing is inversely proportional to the cubic root of the modal volume. Our work completes the kink-vortex-monopole trilogy of zero modes and provides the largest free spectral range for sizable resonators.

Topological physics can be largely understood through the celebrated Dirac equations [1, 2], where the gapped massive solutions correspond to the topological insulators in the bulk and the mid-gap zero-energy solutions correspond to the gapless states at the interfaces. The simplest zero mode is the one-dimensional (1D) kink solution obtained by Jackiw and Rebbi [3], in which the Dirac mass forms a domain wall in real space — the topological defect in 1D. The kink solution has materialized in polyacetylene whose lattice theory is the famed Su-Schrieffer–Heeger model [4]. The 2D topological defect, of Dirac masses, is a vortex whose zero-mode solution was solved by Jackiw and Rossi [5]. These vortex zero modes are proposed both in graphene with Kekulé distortions [6] and in the vortex cores between the superconductor and topological insulator [7]. The graphene model has recently led to experimental realizations of the vortex mid-gap modes in a number of phononic [8–10] and photonic [11–13] lattices. In 3D, however, the dimension of our real world in which the Dirac equation was originally written, no progress has been made towards the physical discovery of the monopole zero mode since its analytical solution was first known in 1976 [3]. In this work, we theoretically propose and experimentally demonstrate this monopole mode in a Dirac crystal using hedgehog modulations as a 3D topological resonator.

The monopole resonator exhibits the best single-mode behaviour ever, i.e., the monopole mode has the largest free-spectral-range (FSR) among all known resonators in the large cavity limit. As discussed in Ref. [13], the mid-gap cavities, of low dimensions, have been established as the ideal robust designs for single-mode selection in semiconductor lasers. The modal spectrum of mainstream diode laser products — powering the Internet communications and cell-phone unlocking — is identical to that of the 1D kink zero modes, whose FSR is inversely proportional to the mode volume. Very recently, the 2D vortex

zero mode inspired the invention of the high-brightness topological-cavity surface-emitting laser [14], whose FSR is inversely proportional to the square root of the mode volume. Now, our 3D monopole resonator, whose FSR is inversely proportional to the cubic root of its mode volume, represents the optimal design for the large-volume single-mode operation.

Jackiw-Rebbi monopole mode

After the proposals of the Dirac monopole in Maxwell’s equations [17] and the ’t Hooft-Polyakov monopole in Yang-Mills equations [18, 19], Jackiw and Rebbi found a zero-mode solution bound to the magnetic monopole in the Dirac equation [2]. The monopole zero mode arises at a 3D topological point defect of three independent mass terms in an 8-by-8 extended Dirac equation shown in Fig. 1. There has to be a minimal of eight bands to allow three mass terms, for the hedgehog construction without breaking the time-reversal symmetry.

We first generalize the Jackiw-Rebbi single-monopole mass profile into the multi-monopole case of arbitrary charges. Although the mass distribution can be chosen to be spherically symmetric for a single monopole, it cannot for monopoles of charge greater than one [20]. Our choice of the spatial mapping of the Dirac-mass vectors $\hat{\mathbf{m}}(\mathbf{r}) = [\hat{m}_x(\mathbf{r}), \hat{m}_y(\mathbf{r}), \hat{m}_z(\mathbf{r})]$ is expressed as

$$\begin{aligned}\hat{m}_x(\mathbf{r}) &= \sin(W_\theta\theta) \cos(W_\phi\phi) \\ \hat{m}_y(\mathbf{r}) &= |\sin(W_\theta\theta)| \sin(W_\phi\phi) \\ \hat{m}_z(\mathbf{r}) &= \cos(W_\theta\theta)\end{aligned}\quad (1)$$

$$W = \frac{1}{8\pi} \int_A dA \epsilon^{\theta\phi} \epsilon^{xyz} \hat{m}_x \partial_\theta \hat{m}_y \partial_\phi \hat{m}_z = W_\theta W_\phi$$

where θ and ϕ are the polar and azimuthal angles in the spherical coordinate; W_θ and W_ϕ are the corresponding

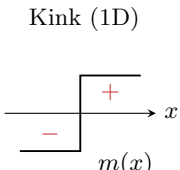
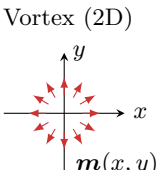
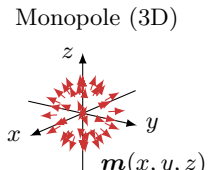
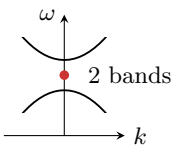
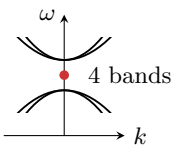
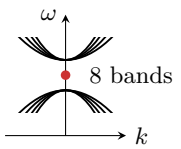
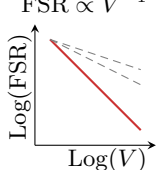
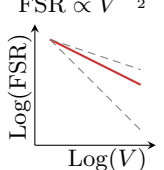
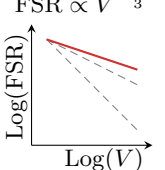
Dirac mass distribution			
Theory	Jackiw-Rebbi (1976)	Jackiw-Rossi (1981)	Jackiw-Rebbi (1976)
Dirac Hamiltonian mass terms	$k_x \sigma_3$ $+m_x \sigma_1 + m' \sigma_2$	$k_x \gamma_{31} + k_y \gamma_{33}$ $+m_x \gamma_{10} + m_y \gamma_{20} + m' \gamma_{32}$	$k_x \Gamma_{331} + k_y \Gamma_{333} + k_z \Gamma_{310}$ $+m_x \Gamma_{100} + m_y \Gamma_{200} + m_z \Gamma_{320} + m' \Gamma_{332}$
Band structure			
Lattice model	SSH (1979)	HCM (2007)	This Work
Resonator device	DFB (1976), VCSEL	TCSEL (2022)	
Free spectral range v.s. mode volume			

FIG. 1. Comparison of topological point defects of the Dirac masses in each dimension. σ_i are the Pauli matrices, $\gamma_{ij} = \sigma_i \otimes \sigma_j$ are the gamma matrices, and $\Gamma_{ijk} = \sigma_i \otimes \sigma_j \otimes \sigma_k$, where \otimes is the Kronecker product. SSH: Su-Schrieffer-Heeger [4], HCM: Hou-Chamon-Mudry [6], DFB: distributed feedback [15], VCSEL: vertical-cavity surface-emitting laser [16], TCSEL: topological-cavity surface-emitting laser [14].

winding numbers. W is the monopole charge, measuring how many times the 3-component Dirac-mass vectors wraps around a closed surface (A) enclosing the monopole [21]. The absolute value in \hat{m}_y , or in \hat{m}_x , ensured that the 3D wrapping number (W) is expressed by the product of the two angular winding numbers. If we use the standard parametrization without the absolute value [22], $W = \frac{1-(-1)^{W_\theta}}{2} W_\phi$. The reason is that the polar angle $\theta \in [0, \pi]$ generates alternating signs of m_z that unwinds each other, while the absolute sign on either m_x or m_y reverses the sign of the in-plane winding wherever m_z unwinds in the polar direction.

In the band-theory language, the above Dirac theory works at the vicinities of the Dirac points in the band structures. The 8-by-8 Dirac equation can be constructed by coupling the two 4-by-4 3D Dirac points. The three mass terms mean three independent ways or perturbations to open the bandgap. In condensed matter, the same low-energy Hamiltonian describes the 3D Majorana zero modes [23, 24], although there has been no clue where to find them. In topological classifications, the kink, vortex, monopole zero modes in 1D, 2D and 3D, localized at the topological defects of Dirac masses, all belong to the same Altland-Zirnbauer symmetry class BDI with integer invariant (\mathbb{Z}) under time-reversal and

chiral symmetries [25]. Of course, the chiral symmetry does not rigorously present in our acoustic system, since the spectrum is not exactly up-down symmetric with respect to the Dirac frequency.

Double 3D Dirac points

The starting point of our design is a crystal hosting two 3D Dirac points to form an 8-by-8 Dirac theory. Our Dirac acoustic crystal is defined by the 3D periodic implicit functions

$$f_D(\mathbf{r}) = \sum_{\text{cyc}} \sin\left(\frac{4\pi}{a}x\right) \cos\left(\frac{2\pi}{a}y\right) \sin\left(\frac{2\pi}{a}z\right) + 3 \sum_{\text{cyc}} \cos\left(\frac{4\pi}{a}x\right) \cos\left(\frac{4\pi}{a}y\right), \quad (2)$$

where a is the lattice constant and \sum_{cyc} is the sum over the cyclic permutation of (x, y, z) . The volume of $f_D(\mathbf{r}) \geq -1.56$ is filled with sound hard material like plastic and the rest volume is air. This lattice geometry, of space group $Ia\bar{3}d$ (#230), is improved upon a previous blue-phase-I (BPI) structure [26–28] to have

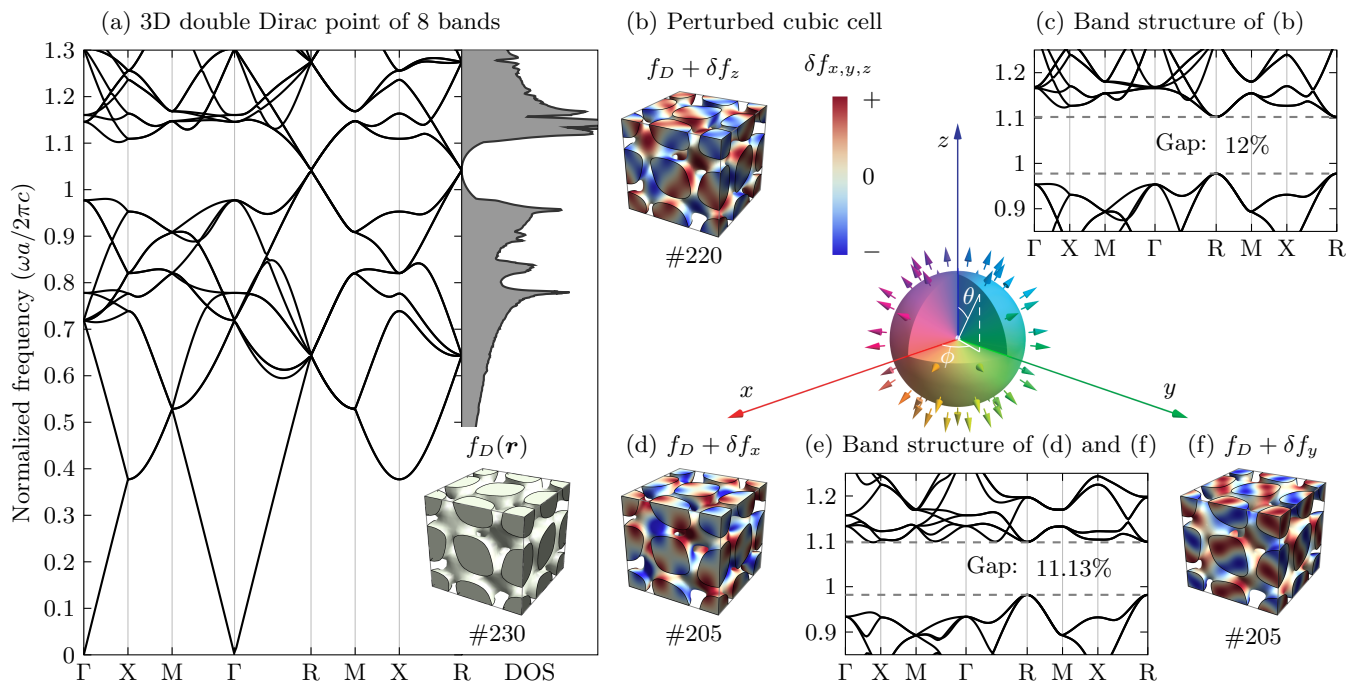


FIG. 2. Acoustic realization of the double Dirac point and the three mass terms for the monopole design. (a) The ideal Dirac acoustic crystal with the 8-band Dirac point in the super cell. (b),(d),(f) The perturbed geometries defined by $f_D(\mathbf{r}) + \delta f_i(\mathbf{r})$, ($i = x, y, z$), whose band structures are plotted in (c) and (e).

two fully frequency-isolated Dirac points, locating at the high-symmetry momenta ($\pm P$) in the Brillouin zone of the body-centered-cubic (BCC) primitive cell. By taking the simple-cubic super-cell as shown in Fig. 2, two Dirac points fold to the momenta R point of the simple-cubic Brillouin zone, forming an 8-by-8 double Dirac point. The corresponding low-energy Dirac Hamiltonian is $k_x\Gamma_{331} + k_y\Gamma_{333} + k_z\Gamma_{310}$ as listed in Fig. 1.

Here we explain a general approach to construct photonic and phononic crystals of a specific space group G using triply periodic functions $F_G(\mathbf{r})$. This is done through a generic Fourier expansion [29] $F_G(\mathbf{r}) = \sum_i [A_i \cos(\mathbf{k}_i \cdot \mathbf{r}) + B_i \sin(\mathbf{k}_i \cdot \mathbf{r})]$ with the real coefficients A_i and B_i , satisfying $F_G(\mathbf{r}) = F_G(g\mathbf{r})$ for each space-group element $g \in G$. The reciprocal lattice vectors $\mathbf{k} = (l\frac{2\pi}{a}, m\frac{2\pi}{b}, n\frac{2\pi}{c})$ are defined by the lattice constant a, b, c and integers l, m, n . One usually takes the lowest l, m, n values for the simplest structures. We use this method to obtain the Dirac structure of Eq. 2 and the symmetry-breaking perturbations (masses) of Eq. 3 to engineer the Dirac masses.

Dirac-mass engineering

In order to build the monopole Dirac-mass field, we need three independent masses out of the total number of four mass terms: $m_x\Gamma_{100}$, $m_y\Gamma_{200}$, $m_z\Gamma_{320}$, and $m'\Gamma_{332}$ as listed in Fig. 1. The latter two are primitive-

cell masses that gaps the individual Dirac point, while the first two are super-cell masses that couple the two Dirac points. All four masses are time-reversal symmetric, while only the first mass (m_x) are inversion symmetric. Through space-group symmetry analysis, we realize all four mass terms by perturbing the improved-BPI acoustic crystal from space group #230 to its subgroups.

The two primitive-cell masses, m_z and m' , are the non-centrosymmetric masses for the individual Dirac point (4-by-4) within the BCC primitive cell. Since #230 has only three maximal BCC subgroups, the non-centrosymmetric #220, #214 (removing inversion) and the centrosymmetric #206 (removing a glide), we conclude that the two primitive-cell mass terms can be realized in #220 and #214 respectively.

The two super-cell masses, the centrosymmetric m_x and the non-centrosymmetric m_y , couple the two Dirac points in the simple-cubic super-cell. The only maximal subgroup of #230, having both a simple-cubic lattice and inversion, is #205 (also a maximal subgroup of #206), reduced from #230 by removing a primitive translation and a glide ($\{M_{01\bar{1}}|(\frac{1}{4}, \frac{1}{4}, \frac{1}{4})\}$), where $M_{01\bar{1}}$ is a mirror operation. Although containing inversion, #205 inherit only half of the inversion centers from #230, in which the two sets of inversion centers are originally connected by the broken glide. Consequently, there are two choices for the symmetry breakings from #230 to #205, in terms of which half of the equivalent inversion centers to preserve. Importantly, these two choices of #205 designs

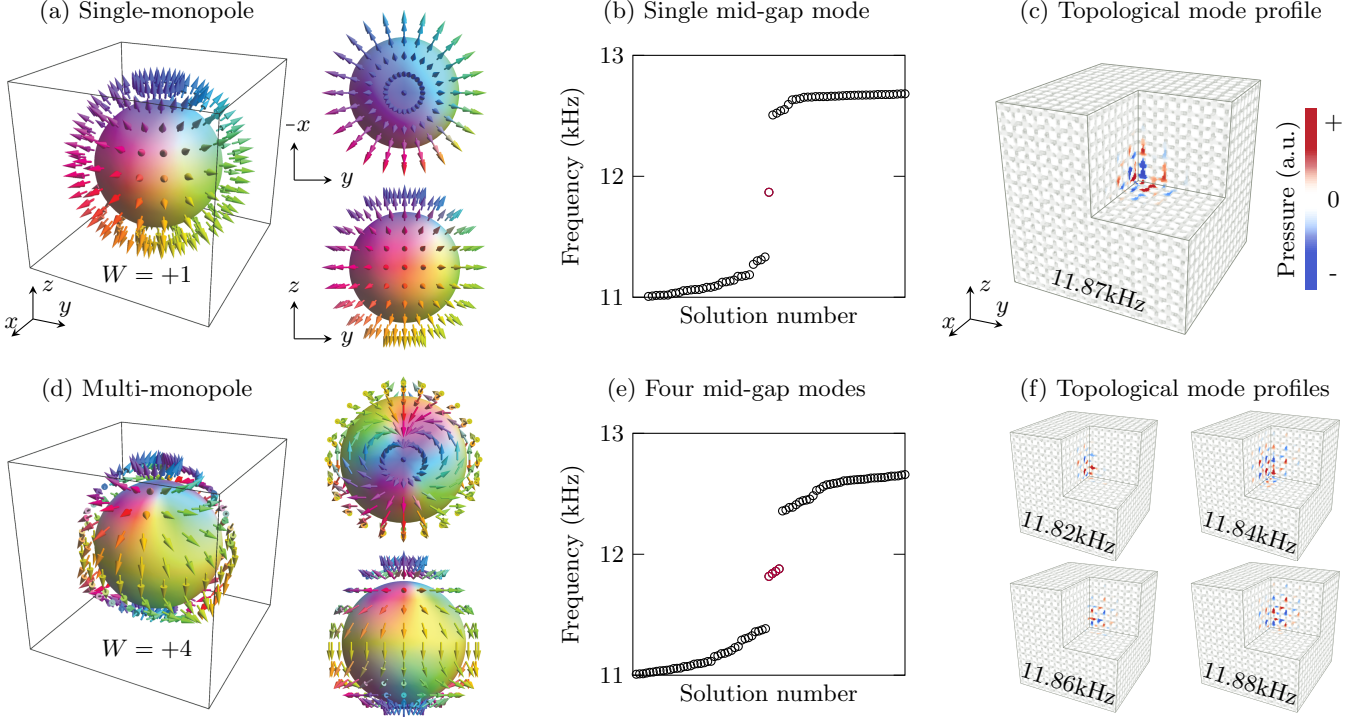


FIG. 3. Single and multi-monopole resonators. (a), (b), (c) Dirac-mass field, eigenvalue spectrum, and the modal field distribution of the single-monopole cavity. (d), (e), (f) Dirac-mass field, eigenvalue spectrum, and the modal field distributions of the multi-monopole cavity with charge four ($W_\theta = W_\phi = +2$).

can be chosen to be the identical structure (Fig. 2d and 2f) related by the glide operation; they correspond exactly to the two super-cell masses (m_x and m_y) in which only one of them is inversion-symmetric. Conceptually, two independent mass terms sharing a symmetry-related identical structure can be understood by considering that two independent masses, forming a complex mass, are related by a phase shift associated with the translation (in the glide). A mass term picking up a phase, through a translation, also occurs in the low-dimensional examples of the SSH model, Dirac-vortex cavity, and one-way fiber [30].

According to the space-group analysis of the four Dirac masses, we realize all of them by imposing the geometric perturbations to the original Dirac-point structure (f_D). These perturbations (δf_x , δf_y , δf_z , $\delta f'$) correspond to the Dirac masses (m_x , m_y , m_z , m') and the required space groups (#205, #205, #220, #214), respectively.

$$\begin{aligned}
 \delta f_x(\mathbf{r}) &= 0.60 \sum_{\text{cyc}} \cos\left(\frac{4\pi}{a}x\right) \sin\left(\frac{4\pi}{a}y\right) \sin\left(\frac{2\pi}{a}z\right) \\
 \delta f_y(\mathbf{r}) &= 0.60 \sum_{\text{cyc}} \sin\left(\frac{4\pi}{a}x\right) \cos\left(\frac{4\pi}{a}y\right) \cos\left(\frac{2\pi}{a}z\right) \\
 \delta f_z(\mathbf{r}) &= 0.36 \sum_{\text{cyc}} \cos\left(\frac{4\pi}{a}x\right) \sin\left(\frac{2\pi}{a}y\right) \cos\left(\frac{2\pi}{a}z\right)
 \end{aligned} \quad (3)$$

The functional forms of the first three perturbations are

listed in Eq. 3, in which the coefficients (amplitudes) are chosen to maximize the size of the common gap as plotted in Fig. 2. It is easy to check that $\delta f_y(\mathbf{r})$ and $\delta f_x(\mathbf{r})$ are related by the glide symmetry $\{M_{011} | (\frac{1}{4}, \frac{1}{4}, \frac{1}{4})\}$ and share the same band structure in Fig. 2 (e). Since $\delta f'$ opens the smallest bandgap, compared with the other three masses, we do not include it for the cavity construction.

Monopole-resonator construction

With three independent mass realizations at hand, we construct the monopole cavity by applying the direction-dependent perturbations to the otherwise uniform 3D Dirac crystal, where $(\delta f_x, \delta f_y, \delta f_z)$ are aligned to the three spatial axes. The geometry of the monopole resonator is defined by:

$$f_D(\mathbf{r}) + \sum_{i=x,y,z} \hat{m}_i(\mathbf{r}, W_\theta, W_\phi) \delta f_i(\mathbf{r}) \geq -1.56 \quad (4)$$

where the hedgehog mass vector $\hat{m}_i(\mathbf{r}, W_\theta, W_\phi)$ is given in equation (1) with the monopole charge $W = W_\theta W_\phi$.

To design the single-monopole cavity, we take $W_\theta = W_\phi = +1$, whose mass field is illustrated in Fig. 3(a). A single mid-gap mode appears in the numerical spectrum in Fig. 3(b), whose frequency deviation from that of the original Dirac point is less than 1%. Plotted in Fig. 3(c)

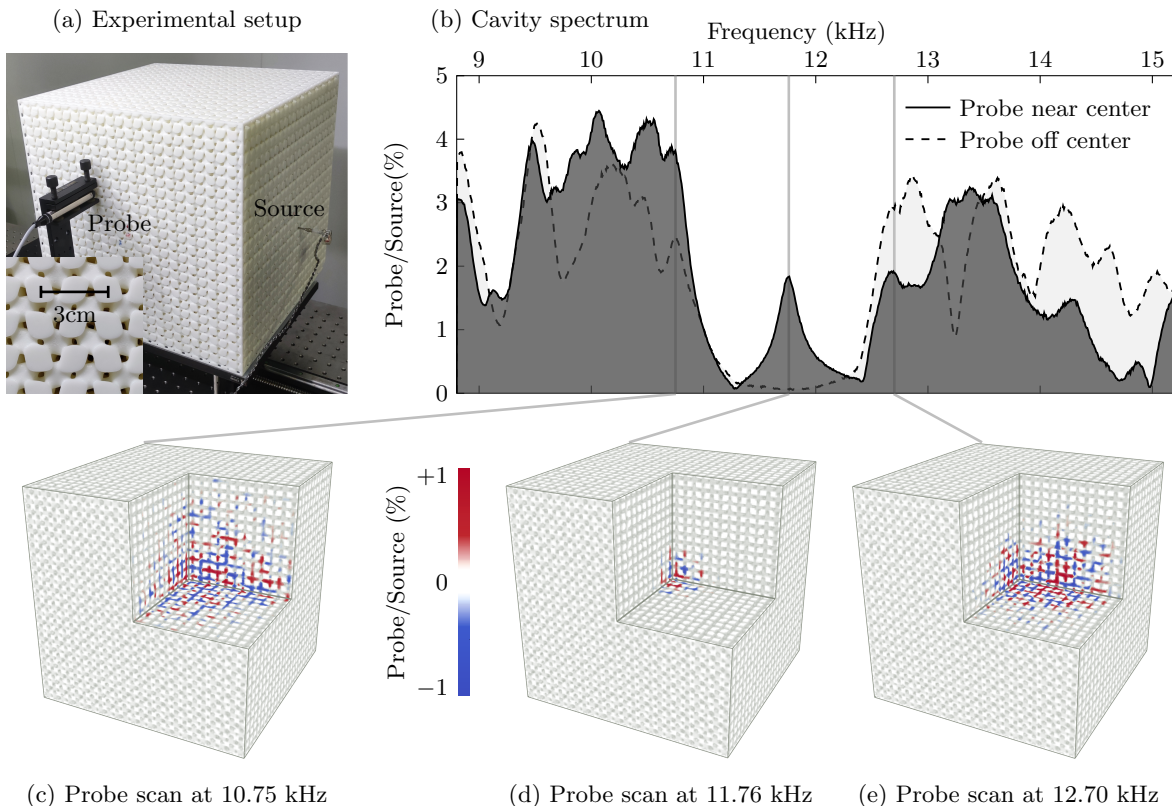


FIG. 4. Experimental results on the monopole resonator. (a) Photograph of experiment setup and a zoom-in of sample surface. The 3D-printed cavity has a lattice constant $a=3$ cm and a sample size of $(12a)^3$. (b) The frequency response of the cavity showing a single mid-gap resonance. (c), (d), (f) Probe scan of the pressure field distributions inside the sample at three resonant peaks across the bandgap.

is the pressure fields of the topological mode localized at the cavity center, with four cubic cells cladded in each direction.

To design the multi-monopole cavity, we take $W_\theta = W_\phi = +2$ with $W = +4$ as an example. The high-charge hedgehog field is illustrate in Fig. 3(d). The numerical results in Fig. 3(e) and (f) show four nearly-degenerate mid-gap modes, whose frequency differences are within 1%.

Acoustic experiments

Encouraged by the simulation results, we 3D-print the acoustic monopole cavity with stereolithography using photo-curable resin. Shown in Fig. 4(a), the sample has a total volume of $(36 \text{ cm})^3$ and a lattice constant of $a=3$ cm. This bi-continuous structure has two types of through holes, separated by 15 mm ($\frac{a}{2}$), whose diameters are about 1.9 mm and 2.8 mm allowing stain-steel tubes to get inside the sample for spectral and spatial measurements. The sound source is an earphone whose output tube tip, diameter of 2.4 mm , is placed near the cavity center. A micro-tube probe (B&K-4182) of diam-

eter 1.2 mm is used to detect the sound pressure any point in the sample. The acoustic signal is a broadband pulse of a 12.0 kHz central frequency and a 6.4 kHz bandwidth, generated and recorded by a signal analysis module (B&K-3160-A-042), the spectrum recorded in each measurement is 100 times averaged.

The two spectra in Fig. 4(b) demonstrate the existence of the bandgap and the localized mid-gap mode. When the probe is off center, the low signal response indicates a bandgap region roughly form 11 kHz to 12.5 kHz . When the probe is centered, a resonate mode peaks in the middle of the gap at 11.76 kHz , whose quality factor is ~ 73 . The field profiles of the resonant modes are mapped out by scanning the probe tube inside the through holes of the sample using a motorized stage. The pressure fields are recorded, with the step size of 7.5 mm ($\frac{a}{4}$), on the three orthogonal surfaces crossing the cavity center. In Fig. 4(c),(d),(e), we plot the signal profiles at the frequencies of the three central resonate modes. It is obvious that only the mid-gap mode is localized as a defect state.

Optimal single-mode behavior

The free spectral range (FSR), of a resonator, is the frequency spacing between adjacent modes that shrinks as the mode volume (V) expands. A wider FSR improves the wavelength-multiplexing bandwidth, the spontaneous emission rate, and the stability of single-mode operations. Although conventional cavities have an inverse proportionality between modal spacing and modal volume ($\text{FSR} \propto V^{-1}$), the recent Dirac-vortex cavity [13] exhibits $\text{FSR} \propto V^{-\frac{1}{2}}$ that drops much slower than the common scaling rule and is ideal for broad-area single-mode lasers [14]. Here we analyze the $\text{FSR}-V$ scaling and show that the monopole cavity of $\text{FSR} \propto V^{-\frac{1}{3}}$ is the optimal.

The FSR is fundamentally related to the density of states $\text{DOS}(\omega_0)$, the number of states in a volume V in a frequency range at the cavity resonance ω_0 . By definition, FSR is the frequency interval across which one extra mode emerges. Since $\text{FSR}/\omega_0 \ll 1$ for large cavities, the function $\text{DOS}(\omega_0 + \text{FSR})$ can be expanded around ω_0 in Taylor series.

$$\begin{aligned} \text{DOS} \cdot \text{FSR} \cdot V &= 1 \\ \text{DOS}(\omega_0 + \text{FSR}) &\propto D_0 + D' \cdot \text{FSR} + D'' \cdot \text{FSR}^2 \dots \end{aligned} \quad (5)$$

where the D_0, D', D'' are the Taylor coefficients. Regular optical media, such as air or uniform dielectrics, has a finite DOS with $D_0 \neq 0$. This is why $\text{FSR} \propto (D_0 \cdot V)^{-1}$ for traditional cavities, such as the Fabry-Perot and whispering-gallery resonators. We note that the scaling power can be lower than -1 if the DOS diverges at a van Hove singularity in photonic crystals, but narrower FSR is not of interest for this discussion.

To beat the inverse scaling law between FSR and V , the cavity mode has to operate at the zero DOS frequency with $D_0 = 0$, at certain (frequency-isolated) bandedge or degeneracy points. For example, the DOS at the linear point degeneracy is $\text{DOS} \propto (\omega - \omega_0)^{\text{dimension}-1}$ in each dimension. Depending on the asymptotic behavior, there are three different cases. 1) $D_0 = 0$ and $D' \neq 0$, so that $\text{FSR} \propto (D' \cdot V)^{-\frac{1}{2}}$. This is the scaling law for 2D Dirac points where the DOS grows linearly with frequency [31]. 2) $D_0 = D' = 0$ and $D'' \neq 0$, so that $\text{FSR} \propto (D'' \cdot V)^{-\frac{1}{3}}$. This is the scaling law for 3D Dirac or Weyl points where the dispersions are all linear and the DOS grows quadratically with frequency. Since the linear dispersion has the lowest DOS in band theory (sublinear band dispersions result in the unphysical divergent group velocities), a further lowering of DOS would mean the bandgap opening in 3D. 3) $D_0 = D' = D'' = 0$, which is the case of a full bandgap in which no mode exists and all Fourier coefficients of $D(\omega_0)$ vanish. Within the bandgap, however, defect modes can exist whose wavefunctions decay in space.

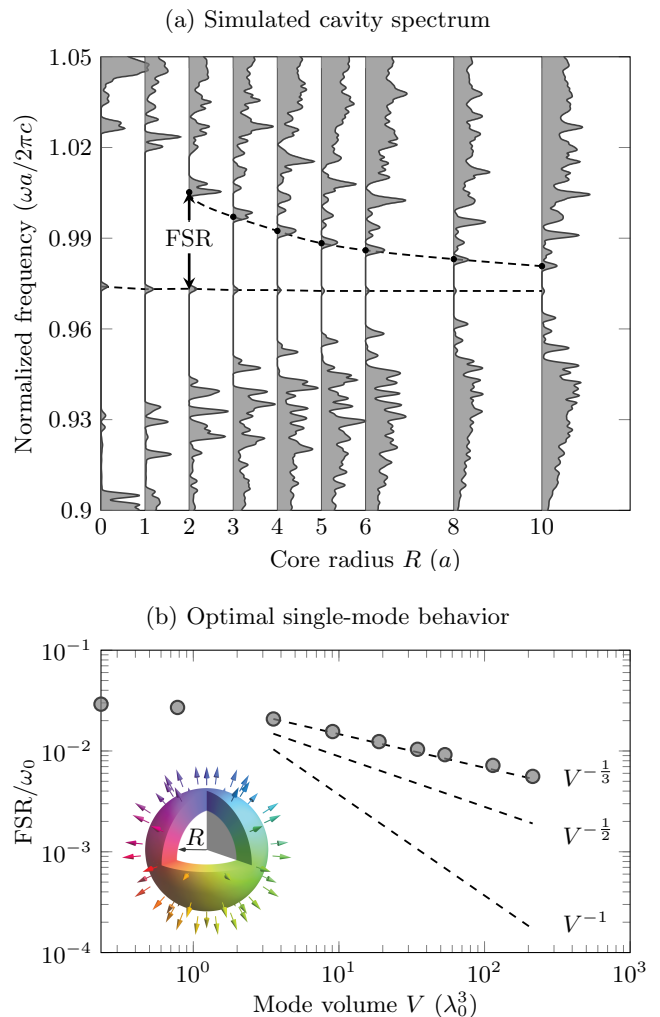


FIG. 5. Numerical demonstration of the optimal $\text{FSR} \propto V^{-\frac{1}{3}}$ scaling of the monopole mode at large volumes. (a) Resonance spectra from the cavities of core radius from 0 to $10a$. The frequency of the monopole mode remains almost a constant at the middle of the bandgaps. (b) Free spectral range versus mode volume relation fitted with the various scaling powers. The inset illustrates the cavity construction with the monopole core radius R .

This DOS analysis is valid for modes of non-decaying wavefunctions, such as the plane wave or Bloch wave, whose modal volume is roughly the cavity size confined by the boundary termination. Interestingly enough, the above analysis for $\text{FSR}-V$ scaling is equally valid for the defect modes of decaying wavefunctions. Because, in the large mode limit, the defect structure disappears into the uniform lattice, as the decay length of the defect mode diverges, and the bandedge (or degeneracy) restores. For example, the quadratic bandedge restores when the depth of the quantum well diminishes and the bound state delocalize. Similarly, the Dirac degeneracy restores when the gap size vanishes and the mid-gap mode evolves into the Bloch mode. Therefore, the large-mode limit of the de-

fect state of decaying wavefunction is precisely the band-edge state of non-decaying wavefunction, where our DOS analysis applies. In summary, the lowest scaling power is always achieved at the linear-dispersion points in each dimension and the best power is $-\frac{1}{3}$ in 3D.

We demonstrate numerically, in Fig. 5, the optimal scaling of the monopole cavity. There are two methods to enlarge the volume of the monopole mode. One method is to lower the bandgap size [14], that is twice the FSR for the mid-gap mode. The other method is to expand the central singular point [13] ($R = 0$) into a volume of unmodulated Dirac lattice with a finite radius R , shown in Fig. 5(b) inset. As R increases, the volume of the mid-gap mode increases and the high-order cavity modes drop into the bandgap. We take this finite- R method, because it requires smaller computational domains and resources. For the same mode volume, the finite- R cavity is more spatially confined, than the $R = 0$ version, due to the non-decaying wavefunction in the gapless core and the fastest decaying tails in the cladding region by choosing the largest bandgap. The $\text{FSR} \propto V^{-\frac{1}{3}}$ relation is clearly identified with the simulation results from $R = 2a$ to $10a$ in Fig. 5(b).

We argue that the monopole resonator is the best design for the large-volume single-mode behavior. Based on the above discussion, it is clear that any cavity of a spectrum converging to a 3D linear dispersion point, in the large cavity limit, shares the optimal scaling of $\text{FSR} = (D'' \cdot V)^{-\frac{1}{3}}$, including the finite-sized periodic Dirac/Weyl crystals. However, the non-topological approaches cannot stabilize a single mode at the center of the Dirac spectrum in the first place. The unique advantage of the monopole cavity is the robust mechanism in pinning a single defect mode at the middle of the bandgap and the gap size can be tuned to zero in a well-controlled fashion.

Conclusion

We experimentally realize the first topological mode in a 3D topological defect, completing the kink, vortex, monopole zero modes in each dimension. The next dimension ahead would be the instanton [32] in 4D space-time. Our approach of constructing the hedgehoges applies to other 3D Dirac/Weyl systems [33–38]. The optimal single-mode behavior of the monopole resonator could enable, in microwave and terahertz, higher-power single-mode masers or lasers.

* linglu@iphy.ac.cn

[1] Shun-Qing Shen. *Topological Insulators: Dirac Equation in Condensed Matter*. Springer, Singapore, 2017.

- [2] Roman Jackiw. Fractional and majorana fermions: the physics of zero-energy modes. *Physica Scripta*, T146:014005, jan 2012.
- [3] Roman Jackiw and Cláudio Rebbi. Solitons with fermion number 1/2. *Physical Review D*, 13(12):3398–3409, 1976.
- [4] W. P. Su, J. R. Schrieffer, and A. J. Heeger. Solitons in polyacetylene. *Phys. Rev. Lett.*, 42:1698–1701, Jun 1979.
- [5] Roman Jackiw and Paolo Rossi. Zero modes of the vortex-fermion system. *Nuclear Physics B*, 190(4):681–691, 1981.
- [6] Chang-Yu Hou, Claudio Chamon, and Christopher Mudry. Electron fractionalization in two-dimensional graphenelike structures. *Phys. Rev. Lett.*, 98:186809, May 2007.
- [7] Liang Fu and C. L. Kane. Superconducting proximity effect and majorana fermions at the surface of a topological insulator. *Phys. Rev. Lett.*, 100:096407, Mar 2008.
- [8] Penglin Gao, Daniel Torrent, Francisco Cervera, Pablo San-Jose, José Sánchez-Dehesa, and Johan Christensen. Majorana-like zero modes in kekulé distorted sonic lattices. *Phys. Rev. Lett.*, 123:196601, Nov 2019.
- [9] Chun-Wei Chen, Natalia Lera, Rajesh Chaunsali, Daniel Torrent, Jose Vicente Alvarez, Jinkyu Yang, Pablo San-Jose, and Johan Christensen. Mechanical analogue of a majorana bound state. *Advanced Materials*, 31(51):1904386, 2019.
- [10] Jingwen Ma, Xiang Xi, Yuan Li, and Xiankai Sun. Nanomechanical topological insulators with an auxiliary orbital degree of freedom. *Nature Nanotechnology*, 16(5):576–583, 2021.
- [11] Adrian J. Menssen, Jun Guan, David Felce, Martin J. Booth, and Ian A. Walmsley. Photonic topological mode bound to a vortex. *Phys. Rev. Lett.*, 125:117401, Sep 2020.
- [12] Jiho Noh, Thomas Schuster, Thomas Iadecola, Sheng Huang, Mohan Wang, Kevin P Chen, Claudio Chamon, and Mikael C Rechtsman. Braiding photonic topological zero modes. *Nature Physics*, 16(9):989–993, 2020.
- [13] Xiaomei Gao, Lechen Yang, Hao Lin, Lang Zhang, Jiafang Li, Fang Bo, Zhong Wang, and Ling Lu. Dirac-vortex topological cavities. *Nat Nanotechnol*, 15(12):1012–1018, 2020.
- [14] Lechen Yang, Guangrui Li, Xiaomei Gao, and Ling Lu. Topological-cavity surface-emitting laser. *Nature Photonics*, 16(4):279–283, 2022.
- [15] H. Haus and C. Shank. Antisymmetric taper of distributed feedback lasers. *IEEE Journal of Quantum Electronics*, 12(9):532–539, 1976.
- [16] Babu Dayal Padullaparthi, Jim Tatum, and Kenichi Iga. *VCSEL Industry: Communication and Sensing*. John Wiley & Sons, 2021.
- [17] Paul Adrien Maurice Dirac. Quantised singularities in the electromagnetic field. *Proceedings of the Royal Society of London. Series A, Containing Papers of a Mathematical and Physical Character*, 133(821):60–72, 1931.
- [18] Gerardus 't Hooft. Magnetic monopoles in unified gauge theories. *Nuclear Physics B*, 79(2):276–284, 1974.
- [19] Alexander M Polyakov. Particle spectrum in the quantum field theory. *JETP Letters*, 20(6):194–195, 1974.
- [20] Erick J. Weinberg and Alan H. Guth. Nonexistence of spherically symmetric monopoles with multiple magnetic charge. *Phys. Rev. D*, 14:1660–1662, Sep 1976.

- [21] Takahiro Fukui and Takanori Fujiwara. Topological stability of majorana zero modes in superconductor–topological insulator systems. *Journal of the Physical Society of Japan*, 79(3):033701, 2010.
- [22] Yakov M. Shnir. *Magnetic Monopoles*. Springer Berlin Heidelberg, Berlin, Heidelberg, 2005.
- [23] Jeffrey CY Teo and Charles L Kane. Majorana fermions and non-abelian statistics in three dimensions. *Phys. Rev. Lett.*, 104:046401, Jan 2010.
- [24] Yusuke Nishida, Luiz Santos, and Claudio Chamon. Topological superconductors as nonrelativistic limits of jackiw-rossi and jackiw-rebbi models. *Phys. Rev. B*, 82:144513, Oct 2010.
- [25] Jeffrey CY Teo and Charles L Kane. Topological defects and gapless modes in insulators and superconductors. *Phys. Rev. B*, 82:115120, Sep 2010.
- [26] Hengbin Cheng, Yixin Sha, Rongjuan Liu, Chen Fang, and Ling Lu. Discovering topological surface states of dirac points. *Phys. Rev. Lett.*, 124:104301, Mar 2020.
- [27] Ling Lu, Chen Fang, Liang Fu, Steven G Johnson, John D Joannopoulos, and Marin Soljačić. Symmetry-protected topological photonic crystal in three dimensions. *Nature Physics*, 12(4):337–U171, 2016.
- [28] Xiangxi Cai, Liping Ye, Chunyin Qiu, Meng Xiao, Rui Yu, Manzhu Ke, and Zhengyou Liu. Symmetry-enforced three-dimensional dirac phononic crystals. *Light: Science & Applications*, 9(1):38, 2020.
- [29] Meinhard Wohlgenuth, Nataliya Yufa, James Hoffman, and Edwin L Thomas. Triply periodic bicontinuous cubic microdomain morphologies by symmetries. *Macromolecules*, 34(17):6083–6089, 2001.
- [30] Ling Lu, Haozhe Gao, and Zhong Wang. Topological one-way fiber of second chern number. *Nature communications*, 9(1):5384, 2018.
- [31] Song-Liang Chua, Ling Lu, Jorge Bravo-Abad, John D. Joannopoulos, and Marin Soljačić. Larger-area single-mode photonic crystal surface-emitting lasers enabled by an accidental dirac point. *Opt. Lett.*, 39(7):2072–2075, Apr 2014.
- [32] Alexander A Belavin, Alexander M , Albert S Schwartz, and Yu S Tyupkin. Pseudoparticle solutions of the yang-mills equations. *Physics Letters B*, 59(1):85–87, 1975.
- [33] NP Armitage, EJ Mele, and Ashvin Vishwanath. Weyl and dirac semimetals in three-dimensional solids. *Rev. Mod. Phys.*, 90:015001, Jan 2018.
- [34] V. Peri, M. Serra-Garcia, R. Ilan, and S. D. Huber. Axial-field-induced chiral channels in an acoustic weyl system. *Nature Physics*, 15(4):357–+, 2019.
- [35] Yihao Yang, Zhen Gao, Haoran Xue, Li Zhang, Mengjia He, Zhaoju Yang, Ranjan Singh, Yidong Chong, Baile Zhang, and Hongsheng Chen. Realization of a three-dimensional photonic topological insulator. *Nature*, 565(7741):622–626, 2019.
- [36] Guancong Ma, Meng Xiao, and C. T. Chan. Topological phases in acoustic and mechanical systems. *Nature Reviews Physics*, 1(4):281–294, 2019.
- [37] Chu-Hao Xia, Hua-Shan Lai, Xiao-Chen Sun, Cheng He, and Yan-Feng Chen. Experimental demonstration of bulk-hinge correspondence in a three-dimensional topological dirac acoustic crystal. *Phys. Rev. Lett.*, 128:115701, Mar 2022.
- [38] Li Luo, Hai-Xiao Wang, Zhi-Kang Lin, Bin Jiang, Ying Wu, Feng Li, and Jian-Hua Jiang. Observation of a phononic higher-order weyl semimetal. *Nature Materials*, 20(6):794–799, 2021.